

# MultiScene: A Large-scale Dataset and Benchmark for Multi-scene Recognition in Single Aerial Images

Yuansheng Hua, Lichao Mou, Pu Jin, and Xiao Xiang Zhu, *Fellow, IEEE*

**Abstract**—Aerial scene recognition is a fundamental research problem in interpreting high-resolution aerial imagery. Over the past few years, most studies focus on classifying an image into one scene category, while in real-world scenarios, it is more often that a single image contains multiple scenes. Therefore, in this paper, we investigate a more practical yet underexplored task—multi-scene recognition in single images. To this end, we create a large-scale dataset, called MultiScene, composed of 100,000 unconstrained high-resolution aerial images. Considering that manually labeling such images is extremely arduous, we resort to low-cost annotations from crowdsourcing platforms, e.g., OpenStreetMap (OSM). However, OSM data might suffer from incompleteness and incorrectness, which introduce noise into image labels. To address this issue, we visually inspect 14,000 images and correct their scene labels, yielding a subset of cleanly-annotated images, named MultiScene-Clean. With it, we can develop and evaluate deep networks for multi-scene recognition using clean data. Moreover, we provide crowdsourced annotations of all images for the purpose of studying network learning with noisy labels. We conduct experiments with extensive baseline models on both MultiScene-Clean and MultiScene to offer benchmarks for multi-scene recognition in single images and learning from noisy labels for this task, respectively. To facilitate progress, we make our dataset and trained models available on <https://github.com/Hua-YS/Multi-Scene-Recognition>.

**Index Terms**—Convolutional neural network (CNN), multi-scene recognition in single images, crowdsourced annotations, large-scale aerial image dataset, learning from noisy labels

## I. INTRODUCTION

With the recent development of Earth observation techniques, massive aerial imagery is now accessible for a variety of applications, such as environmental monitoring [1]–[6], urban planning [7]–[12], land cover and land use mapping [13]–[16], and disaster assessment [17], [18]. As one of the crucial steps towards these applications, aerial scene recognition has been extensively studied in the remote sensing community.

This work is jointly supported by the European Research Council (ERC) under the European Union’s Horizon 2020 research and innovation programme (grant agreement No. [ERC-2016-StG-714087], Acronym: *So2Sat*), by the Helmholtz Association through the Framework of Helmholtz AI [grant number: ZT-I-PF-5-01] - Local Unit “Munich Unit @Aeronautics, Space and Transport (MASTr)” and Helmholtz Excellent Professorship “Data Science in Earth Observation - Big Data Fusion for Urban Research” and by the German Federal Ministry of Education and Research (BMBF) in the framework of the international future AI lab “AI4EO – Artificial Intelligence for Earth Observation: Reasoning, Uncertainties, Ethics and Beyond” (Grant number: 01DD20001). (Corresponding authors: Lichao Mou and Xiao Xiang Zhu.)

Y. Hua, L. Mou, and X. X. Zhu are with the Remote Sensing Technology Institute, German Aerospace Center, 82234 Weßling, Germany, and also with the Data Science in Earth Observation, Technical University of Munich, 80333 Munich, Germany. (e-mails: yuansheng.hua@dlr.de; lichao.mou@dlr.de; konrad.heidler@dlr.de; xiaoxiang.zhu@dlr.de)

P. Jin is with the Data Science in Earth Observation, Technical University of Munich, 80333 Munich, Germany. (e-mail: pu.jin@tum.de)



(a) Single-scene recognition

(b) Multi-scene recognition

Fig. 1. Examples of images utilized in (a) single-scene and (b) multi-scene recognition tasks. In (a), each aerial image is assigned one scene label, while in (b), labels of all present scenes are inferred. In comparison with (b), (a) might suffer from partial scene understanding, as only one label is predicted even if there indeed exist multiple scenes in an image. For a clear visualization, locations of scenes are marked in (b).

During the last few years, the emergence of deep convolutional neural networks (CNNs) pushed ahead research in this field, and enormous achievements [19]–[26] have been obtained. Albeit successful, most existing scene classification researches only focus on a specific scenario, where an aerial image is assumed to include a single scene [27]–[34]. Basically, these studies regard aerial scene recognition as a single-label classification problem and learn models on well-cropped single-scene aerial images (see Fig. 1(a)). However, in practical applications, an aerial image often contains multiple scenes, as it is collected overhead and usually has a large coverage (cf. Fig. 1(b)). We also note that even in public single-scene aerial image datasets, the coexistence of multiple scenes in a single image is inevitable, especially in images covering large areas. For example, as shown in the bottom two images in Fig. 1(a), although they are assigned single scene labels according to their central/dominant scenes (i.e., river and train station), there actually exists more than one scene in each of them.

Hence, in this paper, we aim to tackle a more realistic yet challenging problem, namely multi-scene recognition in single aerial images. This task refers to assigning an aerial image multiple scene labels, and there are no constraints on image preparations, such as centering dominant scenes and eliminating clutter scenes. Compared to the conventional scene recognition task, multi-scene recognition is more arduous because 1) images are large-scale and unconstrained, and 2) all present scenes in an aerial image need to be exhaustively

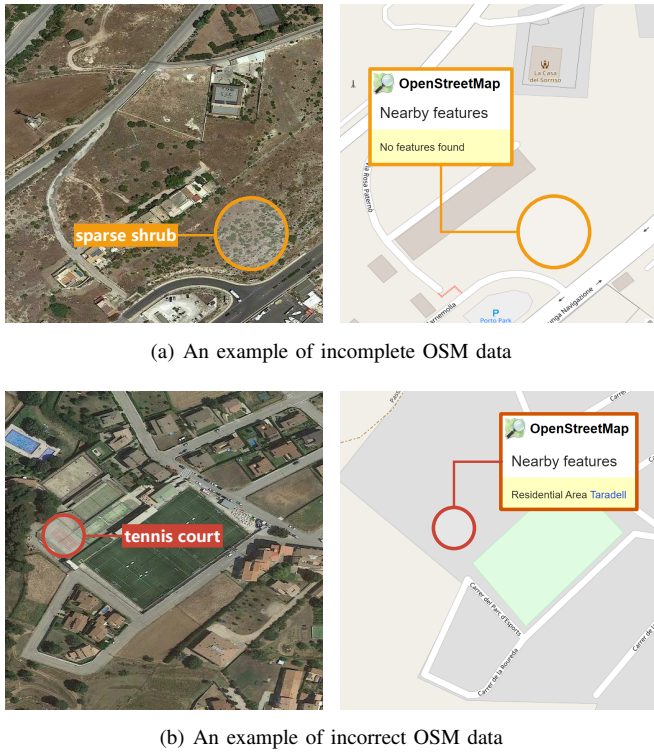


Fig. 2. Examples of (a) incomplete and (b) incorrect OSM annotations. In (a), sparse shrubs are not annotated in OSM data, while in (b), the tennis court is mislabeled as residential.

recognized. Fig. 1(b) shows an example of multi-scene aerial image and corresponding multiple scene-level labels. We can see that not only dominant scenes (e.g., residential and woodland) but also trivial scenes (e.g., bridge and parking lot) are annotated, which draws a more comprehensive picture for the unconstrained image.

However, very few efforts have been deployed to this problem in the remote sensing community. In order to advance the progress of multi-scene recognition in single images, we propose a large-scale Multi-Scene recognition (MultiScene) dataset, where 100,000 aerial images are collected around the world. In the phase of data preparation, we note that although massive high-resolution aerial images can be effortlessly obtained from remote sensing data platforms, such as Google Earth <sup>1</sup>, it is extremely time- and labor-consuming to yield their corresponding multiple scene labels. To alleviate such annotation burden, in this paper, we resort to crowdsourced data, e.g., OpenStreetMap <sup>2</sup> (OSM) annotations, which has been proven to be successful in generating image-level labels [27], [28], [35] and pixel-wise footprints [12], [36] for training deep networks. However, we observe that OSM data might suffer from two common defects, incompleteness and incorrectness, which could introduce severe noise into image labels. Fig 2 shows two examples of incorrect OSM annotations, where (a) sparse shrubs are neglected, and (b) the tennis court is mislabeled as residential. With this in mind, here we do not directly use crowdsourced labels as ground truth

data. Instead, we visually inspect 14,000 images and correct their labels, producing a subset of cleanly-labeled images, named MultiScene-Clean. It allows developing and evaluating deep networks for unconstrained multi-scene recognition using clean data. Moreover, we note that the noisy crowdsourced data are not completely useless, for example, they can be used to study network learning with noisy labels for this task. Therefore, we also provide crowdsourced annotations of all images.

The contributions of this paper are four-fold:

- Unlike conventional aerial scene recognition where all images are well-cropped and each of them contains only one scene-level label, in this paper, we explore a more practical task—multi-scene recognition in single images.
- We propose a large-scale dataset, namely MultiScene, consisting of 100,000 unconstrained multi-scene aerial images, and each is assigned OSM labels. We visually inspect 14,000 images and correct their labels, yielding a subset of cleanly-labeled images.
- The proposed dataset provides not only ground truth data but also crowdsourced labels, which enables researches in learning from enormous noisy labels for our task.
- We extensively evaluate commonly-used classification networks on both MultiScene-Clean and MultiScene and provide benchmarks for recognizing multiple scenes in single images and learning from noisy labels for this task, respectively.

The remaining sections of this paper are organized as follows. Section II reviews studies in aerial single-scene classification and multi-label object classification. Section III briefly recalls existing scene datasets and delineates the proposed dataset. Experimental configurations and results are exhibited in Section IV, and Section V draws a conclusion.

## II. RELATED WORK

This section briefly reviews related works in two fields: aerial single-scene classification and multi-label object recognition.

### A. Aerial Single-scene Classification

Aerial single-scene classification refers to categorize an aerial image into a single scene class. Early researches propose to construct scene representations with variant low-level features, e.g., local structures [41], [42], color attributes [43], [44], and texture information [45], [46]. Concerning that low-level features fail to comprehensively depict complex scenes, mid-level algorithms, such as Bag-of-Visual-Words (BoVW) [47], [48] and topic models [49], [50], are devised to encode local features (so-called “visual words”) into more holistic mid-level scene representations for the classification task. However, these methods show limited performance in recognizing scenes of high diversity due to their dependency on hand-crafted features.

Recently, the emergence of deep CNNs brings immense advancements to the community, and many achievements [19]–[34] have been obtained in the field of aerial single-scene classification. These deep networks have hierarchical architectures,

<sup>1</sup><https://earth.google.com/web/>

<sup>2</sup><https://www.openstreetmap.org/>

TABLE I  
COMPARISON WITH EXISTING AERIAL SCENE DATASETS FROM VARIOUS PERSPECTIVES.

| Dataset                  | # images | spatial resolutions | # scenes | # labels per image | crowdsourced label | Year |
|--------------------------|----------|---------------------|----------|--------------------|--------------------|------|
| UC-Merced [37]           | 2,100    | 0.3 m/pixel         | 21       | 1                  | ×                  | 2010 |
| WHU20 [38]               | 5,000    | 0.3-7.4 m/pixel     | 20       | 1                  | ×                  | 2015 |
| RSSCN7 [39]              | 2,800    | 0.2-1.4 m/pixel     | 7        | 1                  | ×                  | 2015 |
| AID [27]                 | 10,000   | 0.5-8 m/pixel       | 30       | 1                  | ×                  | 2017 |
| NWPU-RESISC45 [40]       | 31,500   | 0.2-30 m/pixel      | 45       | 1                  | ×                  | 2017 |
| <b>MultiScene (Ours)</b> | 100,000  | 0.3-0.6 m/pixel     | 36       | 1-13               | ✓                  | 2021 |

where convolutional and max-pooling layers are periodically interleaved for learning high-level features of intricate scenes. With layers going deeper, the learned features are more abstract and supposed to contain richer semantic information, which is crucial for judicious decisions. A popular trend of deep learning algorithms in single-scene classification is to take a CNN as the backbone and introduce well-designed modules for further enhancing the feature efficiency. For instance, Bi et al. [31] propose to learn multiple instances from feature maps extracted by a densely-connected CNN and integrate them into bag-level features for single-scene classification. Li et al. [51] propose a key region capturing method to learn class-specific features and retain global information for inferring scene labels. To leverage features of variant levels, feature aggregation plays a key role in single-scene classification. Lu et al. [52] fuses features learned by the last three blocks and the second fully-connected layer of VGG-16, and Cao et al. [53] designs a non-parametric self-attention layer to enhance spatial and channel responses of fused features for the final prediction. In [20], the authors develop a gated bidirectional network for aggregating features extracted by different convolutional layers with a gated function in both top-down and bottom-up directions. Besides, exploiting supplementary data, such as geo-tagged audios and multi-temporal images, has been a new research direction. Hu et al. [19] propose to predict scene categories by transferring sound event knowledge learned from sound-image pairs. In [25], the authors propose a two-branch network to learn deep features of bi-temporal images and fuse them through a CorrFusion module for aerial scene classification. Our literature review demonstrates that most of the existing researches assume that an aerial image includes only one scene and focus on well-cropped single-scene aerial images. Hence, these studies tend to regard entities present in an image as compositions of a scene, while in multi-scene recognition, this would trigger networks to learn erroneous feature representations. However, very few efforts have been deployed to explore multi-scene recognition in the remote sensing community.

### B. Multi-label Object Classification

Multi-label object classification refers to assigning an aerial image multiple object-level labels, such as car, tree, and building. Similar to our work, these studies aim to provide a holistic understanding of aerial images, but from the perspective of object. Early attempts [54], [55] follow the idea of simply combining a deep CNN with a post-processing approach for identifying multiple objects in an aerial image. In [54], the authors feed outputs of a CNN into a customized

thresholding operation for inferring multiple object labels, while in [55], a conditional random field (CRF) is utilized as the post-processing model. In recent literature, more efforts are deployed to endow deep neural networks with the capacity of reasoning about relations among various objects for more accurate predictions. In [56], the authors propose an end-to-end network comprising a CNN and a long short-term memory (LSTM) network that is responsible for modeling label dependencies through its recurrent units for multi-label object classification. [57] exploits a bidirectional LSTM network to learn spatial relations among all patches in an image for the final prediction. In [58], the authors propose a relational reasoning network module to model label dependencies and gains better classification results. Instead of encoding label relations, [59] divides an aerial image into several patches with the same size and models spatial relationships among them for multi-label object interpretation. Compared to these researches, our task is more challenging, because compared to object, the concept of scene is more abstract and intricate.

## III. MULTISCENE DATASET FOR MULTI-SCENE RECOGNITION IN SINGLE AERIAL IMAGES

This section first reviews existing single-scene aerial image datasets and then delineates the proposed dataset.

### A. Existing Single-scene Aerial Image Dataset

During the last decades, various aerial image datasets are published for single-scene classification, and here we briefly review several commonly used ones.

- *UC-Merced [37]*: The UC-Merced dataset is composed of 2,100 images collected from the United States Geological Survey (USGS) National Map, and each of them is categorized into one of 21 scene classes: overpass, golf course, river, harbor, beach, building, airplane, freeway, intersection, medium residential, runway, agricultural, storage tank, parking lot, forest, sparse residential, chaparral, tennis courts, dense residential, baseball diamond, and mobile home park. The number of images per scene is evenly defined as 100, and only cities in the United States are covered in data acquisition. The size of each image is  $256 \times 256$  pixels, and the spatial resolution is one foot. In [60], the authors focus on the task of recognizing multiple objects in an image and relabel the UC-Merced dataset, yielding a multi-label dataset. In this dataset, 2,100 images are relabeled, and each is assigned one or several labels from 17 newly defined object classes: airplane, sand, pavement, building, car, chaparral, court,



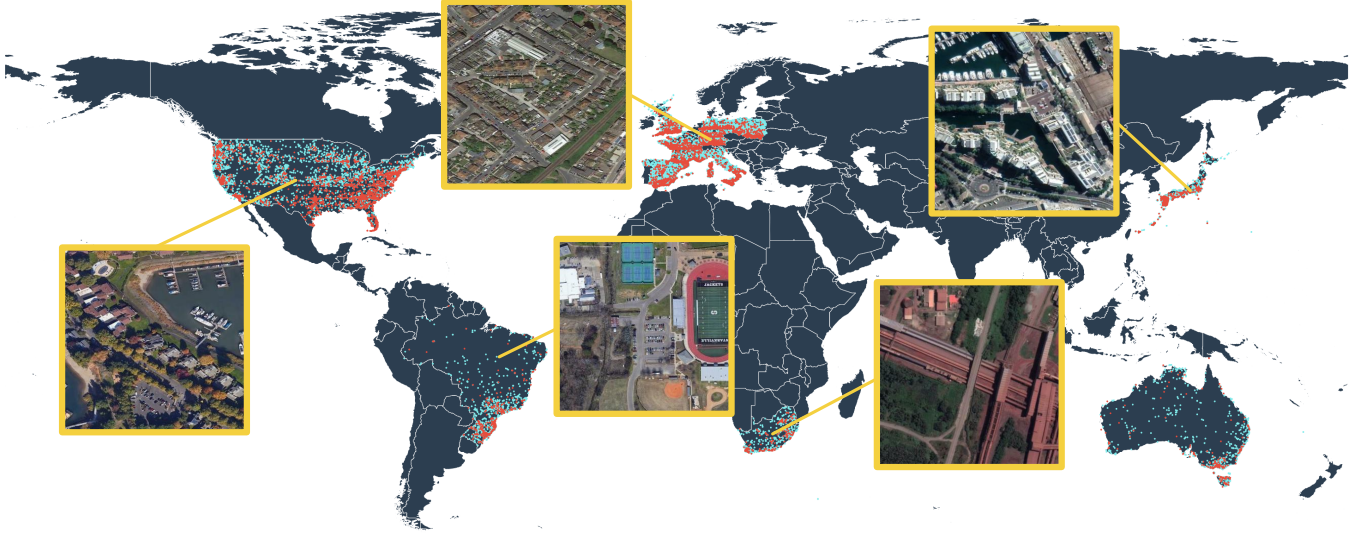


Fig. 3. Coordinate distributions and examples of multi-scene aerial images in our dataset. Red dots denote images with both crowdsourced and clean labels, and cyan dots represent images with only crowdsourced scene labels.

tree, dock, tank, water, grass, mobile home, ship, bare soil, sea, and field.

- **WHU20 [38]:** The WHU20 dataset is an extended version of the WHU-RS dataset that was originally proposed in [61]. This dataset expands numbers of aerial images and scene classes from 950 to 5,000 and from 12 to 20, respectively. For each scene category, more than 200 images with a size of  $600 \times 600$  pixels are collected, and their spatial resolutions range from 0.26 m/pixel to 7.44 m/pixel.
- **RSSCN7 [39]:** The RSSCN7 dataset is a collection of 2,800 high-resolution images each belonging to one of 7 scene categories: grassland, forest, farmland, parking lot, river/lake, industrial region, and residential region. 400 images with different spatial resolutions are cropped from Google Earth imagery for each scene, and the image size is  $400 \times 400$  pixels.
- **AID [27]:** The AID dataset is a large-scale benchmark consisting of 10,000 aerial images and 30 scene types: airport, pond, forest, baseball field, resort, bare land, center, beach, bridge, commercial, desert, storage tanks, farmland, industrial, mountain, park, parking, playground, viaduct, church, railway station, river, school, meadow, sparse residential, dense residential, medium residential, square, stadium, and port. Google Earth is exploited to acquire image samples, and the spatial resolution of each sample varies from 0.5 m/pixel to 8 m/pixel. The size of images is  $600 \times 600$  pixels, and the number of images for each class ranges from 220 to 420.
- **NWPU-RESISC45 [40]:** The NWPU-RESISC45 dataset contains 31,500 high-resolution images and each is assigned with one of 45 scene labels. For each scene, 700 images with a size of  $256 \times 256$  pixels are acquired from Google Earth imagery, and their spatial resolutions vary from 0.2 m/pixel to 30 m/pixel.

In addition, we note that BigEarthNet [62] is a large-

scale dataset for multi-label learning, where 590,326 Sentinel-2 images are captured over the European Union, and their spatial resolutions range from 10 m/pixel to 60 m/pixel. Since BigEarthNet focuses on land covers instead of scenes, we do not specify it here. Table I presents an overview of public high-resolution aerial image datasets from the perspectives of dataset scales, image resolutions, scene categories, and annotations.

### B. MultiScene for Multi-scene Recognition

Although there are already variant datasets for aerial scene recognition, most of them can only be used for single-scene classification. In this paper, we aim to take a step towards a more general scenario, multi-scene recognition in single images, and produce the MultiScene dataset.

To be more specific, we collect 100,000 high-resolution aerial images from Google Earth imagery, which cover six continents, Europe, Asia, North America, South America, Africa, and Oceania, and eleven countries including Germany, France, Italy, England, Spain, Poland, Japan, the United States, Brazil, South Africa, and Australia (cf. Fig. 3). This can ensure high intra-class diversity, as different scene appearances resulted from different cultural regions are covered. The spatial resolution of each image ranges from 0.3 m/pixel to 0.6 m/pixel, and the spatial size of images is  $512 \times 512$  pixels. In contrast to single-scene image datasets [27], [37]–[39], we put no constraints on the location and area of the dominant/trivial scene in an image during the data collection process. Some example multi-scene images are exhibited in Fig. 4. In total, 36 scene categories are defined: apron, baseball field, basketball field, beach, bridge, cemetery, commercial, farmland, woodland, golf course, greenhouse, helipad, lake/pond, oil field, orchard, parking lot, park, pier, port, quarry, railway, residential, river, roundabout, runway, soccer field, solar farm, sparse shrub, stadium, storage tanks, tennis court, train station, wastewater, plant, wind turbine, works, and sea.

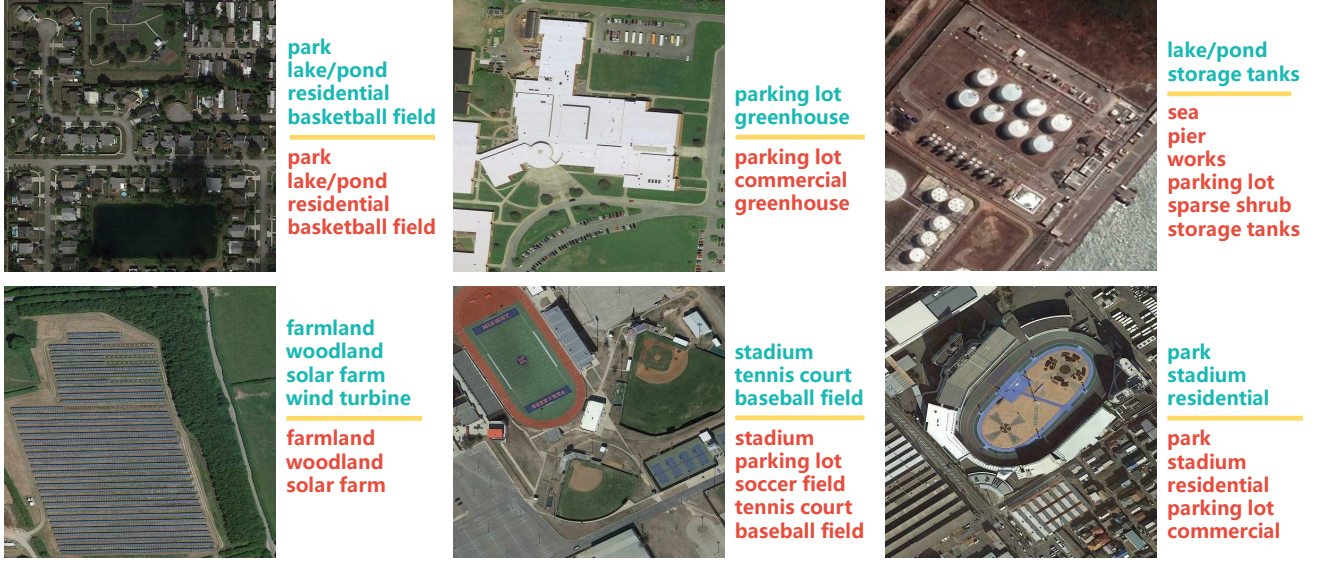


Fig. 4. Example multi-scene aerial images with their crowdsourced and clean annotations in the MultiScene dataset.

To obtain crowdsourced annotations, we first localize each image in OSM with coordinates of its four corners. Afterwards, we parse properties of scenes present in the corresponding region and label images accordingly. In this way, crowdsourced annotations of all aerial images can be automatically yielded at a very low cost compared to conventional manual labeling. However, these almost free annotations might suffer from noise as aforementioned in Section I, and the performance of networks directly trained on them could be degraded. Therefore, we visually inspect 14,000 images from all six continents and correct their labels, yielding a subset, MultiScene-Clean. Fig. 3 shows the coordinate distribution of all images, and the number of samples associated with each scene is present in Fig. 5. Compared to other scene recognition datasets (cf. Table I), our dataset is featured by its manifold labels per image and the available crowdsourced annotations. Fig. 6 further shows the number of images associated with different numbers of scenes.

### C. Challenges

Compared to existing aerial scene datasets, our dataset brings more challenges to the field of scene interpretation from the following three perspectives:

- Images are unconstrained and large-scale, and thus scenes are likely to be incomplete and trivial, which makes recognition more difficult.
- The long-tail sample distribution (see Fig. 5) poses a challenge of learning unbiased models on an imbalanced dataset.
- We gather images from different cultural regions, which results in a high intra-class variation.

## IV. EXPERIMENTS

### A. Experimental Setup

**Data Configuration.** We evaluate the performance of existing models on both MultiScene-Clean and MultiScene

datasets. As to the former, we use 7,000 cleanly labeled images to train and validate networks, and the remaining images are utilized to test networks. For the latter, we leverage the same test set but train deep neural networks on the other 93,000 images with only crowdsourced annotations.

**Evaluation.** For a comprehensive evaluation, we measure the performance of baseline models with class-based, example-based, and overall metrics. Let  $L$  and  $N$  be numbers of classes and examples<sup>3</sup>, these metrics are calculated as follows.

- *Class-based Metrics:* Mean class-based precision (mCP), recall (mCR),  $F_1$  (mCF<sub>1</sub>) score, and per-class average precision (AP) are calculated for measuring the performance of networks from the perspective of class. Specifically, mCP, mCR, and mCF<sub>1</sub> score are computed as:

$$\begin{aligned} \text{mCP} &= \frac{1}{L} \sum_{c=1}^L \frac{\text{TP}_c}{\text{TP}_c + \text{FP}_c}, \quad \text{mCR} = \frac{1}{L} \sum_{c=1}^L \frac{\text{TP}_c}{\text{TP}_c + \text{FN}_c}, \\ \text{mCF}_1 &= \frac{1}{L} \sum_{c=1}^L \frac{\text{TP}_c}{\text{TP}_c + \frac{1}{2}(\text{FP}_c + \text{FN}_c)}, \end{aligned} \quad (1)$$

where  $\text{TP}_c$ ,  $\text{FN}_c$ , and  $\text{FP}_c$  represent numbers of true positives, false negatives, and false positives with respect to the  $c$ -th class, respectively. As to the per-class AP, we first rank all examples according to the predicted probability of the  $c$ -th class in each of them. Then we calculate the corresponding AP with the following formula:

$$\text{AP} = \frac{1}{N_c} \sum_{k=1}^N \frac{\text{TP}_c@k}{\text{TP}_c@k + \text{FP}_c@k} \times \text{rel}@k, \quad (2)$$

where  $N_c$  denotes the number of examples including the  $c$ -th class, and  $\text{TP}_c@k$  and  $\text{FP}_c@k$  represent numbers of true and false positives in top- $k$  examples, respectively.

<sup>3</sup>An example indicates an image which has multiple labels.

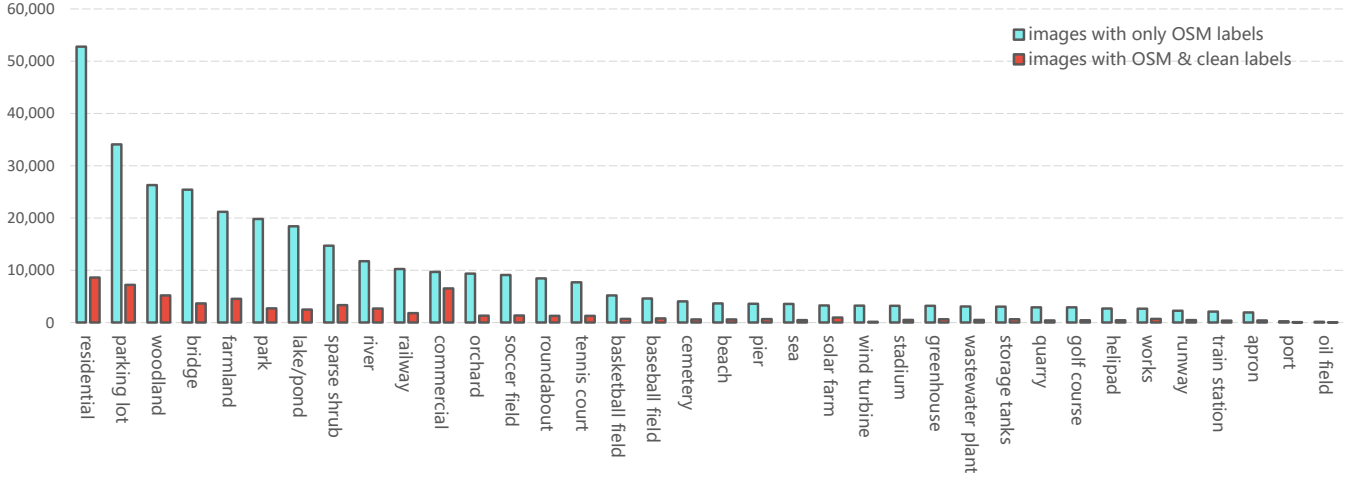


Fig. 5. Sample distributions of all scene categories in our dataset. Each cyan bar indicates the number of images assigned only OSM labels with respect to each scene category, and red bars represent numbers of images with both OSM and clean labels.

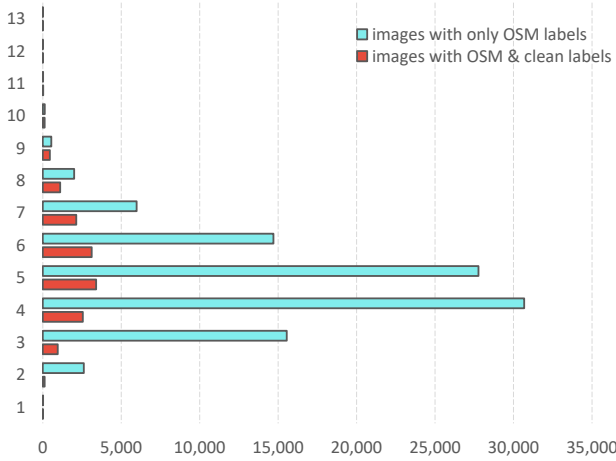


Fig. 6. The number of images associated with different numbers of scenes. Y-axis indicates the number of scenes, and X-axis represents the number of images. The legend is the same as that in Fig. 5.

Notably,  $TP_c@k$  and  $FP_c@k$  are equivalent to  $TP_c$  and  $FP_c$ , when  $k$  equals to  $N$ .  $rel@k$  denotes the relevance between the  $k$ -th example and the  $c$ -th class, and it is set to 0/1 when the  $c$ -th class is included/excluded. Besides, the mean average precision (mAP) can be computed by averaging APs for all categories.

- **Example-based Metrics:** Mean example-based precision (mEP), recall (mER), and  $F_1$  (mEF<sub>1</sub>) score are computed to validate networks from the perspective of example with the following equations:

$$\begin{aligned} mEP &= \frac{1}{N} \sum_{k=1}^N \frac{TP_k}{TP_k + FP_k}, \quad mER = \frac{1}{N} \sum_{k=1}^N \frac{TP_k}{TP_k + FN_k}, \\ mEF_1 &= \frac{1}{N} \sum_{k=1}^N \frac{TP_k}{TP_k + \frac{1}{2}(FP_k + FN_k)}, \end{aligned} \quad (3)$$

where  $TP_k$ ,  $FP_k$ , and  $FN_k$  denote numbers of true positives, false positives, and false negatives in the  $k$ -th

example.

- **Overall Metrics:** Overall precision (OP), recall (OR), and  $F_1$  (OF<sub>1</sub>) score can be used to measure the performance of models from a more holistic perspective, and they are calculated as:

$$\begin{aligned} OP &= \frac{TP}{TP + FP}, \quad OR = \frac{TP}{TP + FN}, \\ OF_1 &= \frac{TP}{TP + \frac{1}{2}(FP + FN)}, \end{aligned} \quad (4)$$

where TP, FP, and FN are counted based on predictions of all scenes and examples.

## B. Baselines

To provide comprehensive benchmarks, we evaluate the performance of extensive popular deep neural networks. Since they were originally designed for single-label classification, we substitute sigmoid functions for their softmax activations to predict multiple scene labels that are encoded into multi-hot binary sequences. Besides, several classical machine learning algorithms are also evaluated. In total, 22 models are tested on both MultiScene-Clean and MultiScene datasets, and a brief review is as follows.

- **SVM [63]:** Support vector machine (SVM) aims to learn one or several hyperplanes for separating samples of different classes with the largest margin. Usually, the hyperplanes are constructed in a high dimensional space, and can be learned directly (Linear SVM) or through kernel functions (Nonlinear SVM). In our experiments, we select the latter and use a radial basis function (RBF) kernel [64] to learn SVM.
- **RF [65]:** Random forest (RF) is an ensemble of decision trees, which are trained with random subspaces of image features and make final predictions through the majority voting. The number of decision trees is set to 200 in our experiments.

TABLE II  
NUMERICAL RESULTS OF BASELINE MODELS ON THE MULTISCENE-CLEAN DATASET (%). MODELS ARE TRAINED AND TESTED ON CLEANLY-LABELLED IMAGES, AND THE BEST SCORES ARE SHOWN IN BOLD.

| Model         | mAP         | mCP         | mCR         | mCF <sub>1</sub> | mEP         | mER         | mEF <sub>1</sub> | OP          | OR          | OF <sub>1</sub> |
|---------------|-------------|-------------|-------------|------------------|-------------|-------------|------------------|-------------|-------------|-----------------|
| SVM           | 14.9        | 19.6        | 8.4         | 8.6              | 62.2        | 32.8        | 41.1             | 66.9        | 32.2        | 43.5            |
| RF            | 15.6        | 25.4        | 8.7         | 9.5              | 64.6        | 32.5        | 41.4             | 70.9        | 32.1        | 44.2            |
| XGBOOST       | 16.9        | 34.1        | 11.2        | 12.8             | 67.0        | 37.4        | 45.8             | 69.6        | 36.5        | 47.9            |
| VGG-16        | 56.5        | 63.3        | 47.9        | 53.6             | 74.9        | 64.3        | 67.0             | 73.6        | 63.1        | 67.9            |
| VGG-19        | 56.4        | 62.9        | 47.7        | 53.3             | 74.8        | 64.1        | 66.8             | 73.5        | 62.7        | 67.7            |
| Inception-V3  | 53.5        | 65.0        | 40.8        | 48.5             | 74.2        | 59.9        | 63.9             | 73.0        | 58.6        | 65.0            |
| ResNet-50     | 62.0        | 74.8        | 45.9        | 55.1             | 79.7        | 62.7        | 67.9             | 79.0        | 61.4        | 69.1            |
| ResNet-101    | 63.0        | 75.9        | 46.6        | 55.8             | 79.9        | 64.3        | 69.1             | 79.2        | 63.1        | 70.3            |
| ResNet-152    | 63.8        | 74.9        | 49.1        | 57.7             | <b>80.8</b> | 64.0        | 69.2             | <b>80.1</b> | 62.8        | 70.4            |
| SqueezeNet    | 46.3        | 58.1        | 36.8        | 43.5             | 71.3        | 58.0        | 61.3             | 70.0        | 56.9        | 62.7            |
| MobileNet-V2  | 58.8        | 70.9        | 44.8        | 53.1             | 77.6        | 62.7        | 67.0             | 76.6        | 61.6        | 68.3            |
| ShuffleNet-V2 | 50.7        | 61.8        | 38.1        | 45.7             | 73.8        | 58.2        | 62.5             | 73.0        | 57.0        | 64.0            |
| DenseNet-121  | 62.2        | 74.6        | 45.1        | 54.4             | 79.5        | 61.8        | 67.3             | 79.1        | 60.6        | 68.6            |
| DenseNet-169  | 63.2        | 76.7        | 45.8        | 55.3             | 80.4        | 63.4        | 68.6             | 79.6        | 62.3        | 69.9            |
| ResNeXt-50    | 63.4        | <b>77.3</b> | 45.0        | 54.2             | 78.5        | 64.3        | 68.6             | 77.8        | 63.2        | 69.8            |
| ResNeXt-101   | <b>64.8</b> | 76.5        | 48.6        | 57.3             | 79.3        | 66.6        | <b>70.2</b>      | 78.5        | 65.4        | <b>71.3</b>     |
| MnasNet       | 53.8        | 61.8        | 42.9        | 49.9             | 73.0        | 59.4        | 63.0             | 72.1        | 58.1        | 64.3            |
| KFBNNet       | 58.8        | 68.8        | 45.2        | 53.3             | 77.9        | 64.2        | 68.1             | 77.3        | 63.0        | 69.4            |
| FACNN         | 56.5        | 60.3        | 48.7        | 52.6             | 73.1        | 65.3        | 66.8             | 71.6        | 64.1        | 67.7            |
| SAFF          | 61.8        | 72.5        | 48.1        | 56.7             | 79.4        | 63.9        | 68.6             | 78.7        | 62.8        | 69.9            |
| LR-VGG-16     | 58.1        | 67.7        | 46.7        | 54.2             | 77.3        | 64.6        | 68.0             | 76.2        | 63.5        | 69.2            |
| LR-ResNet-50  | 63.1        | 68.1        | <b>53.1</b> | <b>59.0</b>      | 76.7        | <b>67.6</b> | 69.7             | 75.3        | <b>66.5</b> | 70.6            |

- *XGBOOST*: XGBOOST<sup>4</sup> is a computationally efficient implementation of gradient-boosted trees [66] that optimizes tree ensembles (e.g., an ensemble of decision trees) through successive learning steps [67]. In each step, the existing trees are fixed, and a new tree is added and optimized with objective functions. Considering the difficulty of our task, we set the number of trees to 200 for training XGBOOST on both datasets.
- *VGGNet* [68]: VGGNet utilizes five convolutional blocks and three fully-connected layers to extract high-level features for image classification. Each block has multiple stacked convolutional layers and ends with one max-pooling layer. The size of convolutional filters is  $3 \times 3$ , and the stride of max-pooling layers is 2. In our experiments, a 16-layer VGGNet (VGG-16) and a 19-layer VGGNet (VGG-19) are trained on our dataset.
- *Inception networks* [69]–[72]: Inception networks are characterized by their wide modules, where convolutional filters of variant sizes and max-pooling operators are jointly employed to learn diverse features. Besides, a bottleneck architecture made of  $1 \times 1$  convolutions is introduced to mitigate the boosted computational cost resulting from heavy inception modules. In Table II and III, we report the performance of Inception-v3 [71] in multi-scene recognition.
- *ResNet* [73]: ResNet aims to address the degradation problem by learning residual mappings with shortcut connections. By doing so, ResNet can go much deeper than plain CNNs and achieve outstanding performance in not only image classification but also semantic segmentation and object detection tasks. In our experiments, we evaluate a 50-layer ResNet (ResNet-50), a 101-layer ResNet (ResNet-101), and a 152-layer ResNet (ResNet-152) on

the proposed dataset. Notably, residual blocks in these deep ResNets are modified into bottleneck architectures for reducing the computational burden.

- *SqueezeNet* [74]: SqueezeNet focuses on preserving network performance with fewer parameters. To achieve this, most of  $3 \times 3$  convolutional filters are replaced with  $1 \times 1$  filters, and features are squeezed in the channel dimension before fed into the remaining  $3 \times 3$  filters. In addition, bypass connections are introduced to features of the same size for improving the classification performance. Experimental results of SqueezeNet on our dataset are reported in Section IV-D and IV-D2.
- *MobileNet* [75]: MobileNet is a light-weight deep neural network, which is applicable on mobile devices with restricted computational sources. The network is designed in a streamlined architecture, and depthwise separable convolutions play a significant role in increasing computational efficiency. Specifically, such convolutions are implemented by factorizing standard convolutions into depthwise and pointwise convolutions. The former is conducted on each channel, and the latter aggregates channel-wise outputs via  $1 \times 1$  convolutions. To further reduce the computational cost, two hyperparameters, width multiplier  $\alpha$  and resolution multiplier  $\beta$ , are designed to shrink feature channels and input resolutions, respectively. In the advanced variation of MobileNet, i.e., MobileNet-V2 [76], inverted residual connections and linear bottlenecks are developed to improve the network performance. In our experiments, we train MobileNet-V2 and set both  $\alpha$  and  $\beta$  as the default value, 1.
- *ShuffleNet* [77]: ShuffleNet improves computational efficiency by utilizing pointwise group convolutions and channel shuffle. Specifically, the former divides feature maps into several groups and conducts  $1 \times 1$  convolutions on each group independently. The latter rearranges feature

<sup>4</sup><https://xgboost.readthedocs.io/en/latest/tutorials/model.html>


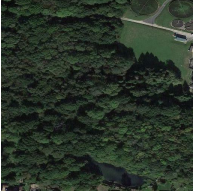






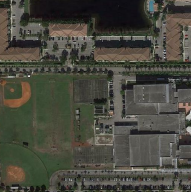



TABLE III  
COMPARISONS OF APS ON THE MULTISCENE-CLEAN DATASET (%). THE BEST APS ARE SHOWN IN BOLD.

| Model         | apron       | baseball field | beach       | bridge      | cemetery    | commercial  | farmland    | woodland    | golf course | greenhouse  | helipad     | lake/pond   | oil field   | orchard     | parking lot | park        | pier        | port        | quarry      | railway     | residential | roundabout  | runway      | soccer field | solar farm  | spare shrub | stadium     | storage tanks | tennis court | train station | wastewater plant | wind turbine | sea works   |             |      |             |
|---------------|-------------|----------------|-------------|-------------|-------------|-------------|-------------|-------------|-------------|-------------|-------------|-------------|-------------|-------------|-------------|-------------|-------------|-------------|-------------|-------------|-------------|-------------|-------------|--------------|-------------|-------------|-------------|---------------|--------------|---------------|------------------|--------------|-------------|-------------|------|-------------|
| SVM           | 3.1         | 6.3            | 5.4         | 4.0         | 29.9        | 4.5         | 60.5        | 44.1        | 55.2        | 3.1         | 5.2         | 3.0         | 18.0        | 0.1         | 9.9         | 65.5        | 20.2        | 5.5         | 0.6         | 3.0         | 13.4        | 68.3        | 19.3        | 8.7          | 3.7         | 9.5         | 8.0         | 25.7          | 3.7          | 5.2           | 9.1              | 2.7          | 3.6         | 0.8         | 5.2  | 3.4         |
| RF            | 3.1         | 6.3            | 5.4         | 10.9        | 28.1        | 4.5         | 62.7        | 53.2        | 54.6        | 3.1         | 5.4         | 3.0         | 17.4        | 0.1         | 10.1        | 65.6        | 20.2        | 7.1         | 0.6         | 3.0         | 13.6        | 73.3        | 19.5        | 8.7          | 3.7         | 9.5         | 10.6        | 26.2          | 3.7          | 4.9           | 9.1              | 2.7          | 3.6         | 0.8         | 5.2  | 3.4         |
| XGBOOST       | 3.1         | 9.4            | 5.4         | 15.8        | 33.4        | 4.5         | 62.8        | 56.2        | 57.6        | 3.1         | 5.2         | 3.0         | 21.5        | 0.1         | 11.5        | 68.8        | 23.3        | 9.3         | 0.6         | 3.0         | 13.8        | 74.7        | 20.3        | 8.7          | 4.2         | 9.8         | 10.9        | 32.9          | 3.7          | 5.2           | 9.1              | 2.7          | 3.6         | 0.8         | 5.2  | 4.3         |
| VGG-16        | 72.2        | 81.7           | 24.2        | 70.0        | 72.1        | 28.9        | 81.6        | 87.8        | 85.7        | 65.1        | 42.8        | 34.9        | 63.2        | 1.9         | 72.0        | 86.2        | 50.1        | 72.7        | 19.0        | 50.9        | 55.6        | 93.7        | 52.5        | 65.8         | 68.7        | 61.6        | 32.4        | 59.7          | 53.7         | 49.4          | 63.6             | 35.5         | 45.9        | 51.6        | 27.2 | 54.9        |
| VGG-19        | 70.1        | 80.7           | 21.3        | 67.1        | 71.7        | 28.0        | 80.6        | 87.4        | 85.5        | 64.5        | 44.4        | 33.5        | 64.1        | 2.6         | 73.4        | 86.6        | 50.7        | 72.4        | 17.2        | 50.7        | 56.4        | 93.8        | 52.3        | 68.7         | 68.6        | 62.3        | 32.3        | 58.2          | 53.0         | 49.1          | 66.8             | 37.6         | 47.0        | 50.3        | 28.3 | 54.5        |
| Inception-V3  | 67.8        | 83.2           | 20.0        | 68.8        | 69.9        | 19.8        | 81.4        | 85.0        | 83.1        | 51.4        | 36.4        | 33.0        | 55.2        | 0.5         | 68.3        | 86.0        | 50.0        | 70.5        | 13.5        | 49.0        | 47.9        | 92.3        | 49.8        | 63.9         | 65.4        | 59.7        | 31.1        | 56.6          | 57.9         | 44.6          | 55.5             | 34.5         | 46.9        | 44.5        | 22.7 | 59.6        |
| ResNet-50     | 77.3        | 86.7           | 26.4        | 79.4        | 74.6        | 39.7        | 83.3        | 88.4        | 86.7        | 76.7        | 49.3        | 43.1        | 66.0        | 0.5         | 76.8        | 88.2        | 55.3        | 77.2        | 24.7        | 55.7        | 62.4        | 94.3        | 59.6        | 71.2         | 74.8        | 67.7        | 40.3        | 61.9          | 63.0         | 55.0          | 68.8             | 46.7         | 54.5        | 50.3        | 36.0 | 68.9        |
| ResNet-101    | 79.7        | 88.0           | 27.6        | 80.2        | 75.9        | 44.5        | 84.2        | 88.4        | 87.3        | 75.6        | 49.7        | 45.3        | 68.7        | 0.9         | 77.8        | 88.6        | 58.3        | 77.6        | 20.9        | 61.2        | 62.7        | 94.5        | 61.5        | 73.3         | 77.4        | 70.0        | 40.0        | 62.1          | 64.6         | 54.2          | 70.9             | 46.6         | 55.8        | 47.2        | 37.8 | 68.1        |
| ResNet-152    | 79.1        | <b>88.6</b>    | 27.4        | <b>84.0</b> | 77.1        | 42.4        | 83.9        | 88.7        | 87.6        | 77.4        | 51.8        | 46.9        | 68.8        | 0.4         | 78.3        | 89.2        | <b>59.4</b> | <b>79.3</b> | 20.3        | 59.4        | 65.1        | 94.5        | 61.9        | 74.4         | 77.7        | 70.7        | 41.0        | 62.8          | 65.1         | <b>57.2</b>   | 72.5             | 51.3         | 57.3        | 48.8        | 35.5 | <b>71.1</b> |
| SqueezeNet    | 51.4        | 73.8           | 18.2        | 57.6        | 59.4        | 15.6        | 77.4        | 83.8        | 81.6        | 50.1        | 34.0        | 12.3        | 51.3        | 0.7         | 65.9        | 83.7        | 44.2        | 56.8        | 20.5        | 34.7        | 46.2        | 93.2        | 44.9        | 57.7         | 58.0        | 45.7        | 27.4        | 53.2          | 38.9         | 35.9          | 56.1             | 22.8         | 26.8        | 18.0        | 18.9 | 49.1        |
| MobileNet-V2  | 74.3        | 84.4           | 24.8        | 78.5        | 73.4        | 32.5        | 81.9        | 87.2        | 85.9        | 72.2        | 46.3        | 38.9        | 64.3        | 1.6         | 73.8        | 88.3        | 53.7        | 72.2        | 18.1        | 51.8        | 60.0        | 93.6        | 55.8        | 71.7         | 67.8        | 64.1        | 34.3        | 60.4          | 58.7         | 46.3          | 69.8             | 40.7         | 47.1        | 48.5        | 31.5 | 64.0        |
| ShuffleNet-V2 | 62.0        | 78.4           | 23.5        | 67.5        | 66.8        | 14.4        | 80.5        | 84.1        | 82.5        | 61.0        | 36.6        | 18.0        | 56.5        | 0.4         | 65.0        | 85.5        | 48.6        | 61.9        | 11.0        | 40.4        | 50.6        | 92.5        | 48.9        | 57.0         | 66.5        | 59.4        | 31.0        | 57.3          | 51.7         | 37.5          | 56.3             | 30.2         | 36.4        | 20.4        | 27.0 | 58.8        |
| DenseNet-121  | 79.0        | 87.5           | 28.3        | 80.9        | 75.1        | 37.9        | 83.5        | 87.7        | 85.5        | <b>78.0</b> | 48.0        | 47.3        | 66.3        | 2.9         | 75.7        | 88.5        | 58.3        | 77.7        | 25.3        | 58.4        | 62.3        | 94.1        | 58.5        | 73.6         | 73.9        | 67.1        | 39.1        | 61.6          | 61.4         | 54.3          | 69.9             | 47.4         | 56.4        | 50.2        | 31.0 | 66.5        |
| DenseNet-169  | 81.8        | 88.1           | 26.3        | 81.4        | 76.9        | 42.6        | <b>84.5</b> | 88.1        | 86.0        | 77.2        | 49.0        | 44.1        | 67.4        | 4.3         | 78.7        | 88.8        | 56.6        | 78.1        | 21.4        | 58.2        | 62.9        | 94.4        | 60.5        | 72.4         | 75.4        | 69.4        | 41.2        | 61.2          | <b>65.9</b>  | 54.6          | 72.4             | 51.4         | 58.6        | 53.2        | 35.1 | 67.6        |
| ResNeXt-50    | 81.5        | 87.1           | 27.6        | 81.6        | 75.5        | 41.3        | 83.4        | 88.2        | 86.3        | 76.1        | 50.8        | 50.3        | 66.3        | 9.6         | 75.3        | 89.0        | 57.6        | 77.7        | 23.8        | 58.6        | 64.5        | 94.1        | 61.4        | 73.3         | 76.7        | 68.7        | 40.9        | 62.2          | 63.5         | 53.8          | 71.8             | 50.2         | 56.9        | <b>54.7</b> | 34.9 | 66.6        |
| ResNeXt-101   | <b>82.3</b> | 87.7           | <b>30.2</b> | 82.9        | <b>77.2</b> | <b>45.6</b> | 84.1        | <b>88.8</b> | 87.3        | 77.1        | <b>52.6</b> | <b>54.8</b> | <b>71.0</b> | 1.3         | <b>79.4</b> | <b>89.7</b> | 58.6        | 76.1        | 20.3        | <b>61.8</b> | <b>66.5</b> | 94.5        | <b>64.3</b> | 75.0         | <b>79.2</b> | <b>72.0</b> | <b>42.3</b> | 63.3          | 64.5         | 55.4          | 75.1             | <b>54.4</b>  | <b>58.7</b> | 52.5        | 37.8 | 67.2        |
| MnasNet       | 69.4        | 84.0           | 21.6        | 70.9        | 67.4        | 20.7        | 78.9        | 84.7        | 82.4        | 63.0        | 42.0        | 27.5        | 58.3        | 0.7         | 70.5        | 85.7        | 49.1        | 69.5        | 18.1        | 45.2        | 51.6        | 91.4        | 48.0        | 66.1         | 66.4        | 59.0        | 33.3        | 55.9          | 53.2         | 42.4          | 61.5             | 32.8         | 42.6        | 33.4        | 25.6 | 62.6        |
| KFBNet        | 68.4        | 83.0           | 27.2        | 75.1        | 75.4        | 37.6        | 82.2        | 88.7        | 86.7        | 68.4        | 47.8        | 47.0        | 67.4        | 6.3         | 75.7        | 89.1        | 55.3        | 73.1        | 10.1        | 57.2        | 58.5        | <b>94.6</b> | 55.1        | 72.5         | 68.7        | 64.7        | 35.4        | 60.3          | 46.5         | 48.5          | 74.8             | 31.6         | 47.3        | 49.1        | 26.0 | 61.2        |
| FACNN         | 69.4        | 83.7           | 21.5        | 70.5        | 72.9        | 31.7        | 81.8        | 88.4        | 85.4        | 66.4        | 36.9        | 36.2        | 65.9        | 4.8         | 72.8        | 87.5        | 50.4        | 71.1        | 12.6        | 57.8        | 54.5        | 93.6        | 55.2        | 70.1         | 68.4        | 64.5        | 32.4        | 56.4          | 50.0         | 50.8          | 68.4             | 32.3         | 46.1        | 46.4        | 23.9 | 54.2        |
| SAFF          | 74.5        | 86.2           | 29.8        | 76.8        | 75.1        | 41.4        | 83.0        | 88.7        | 86.6        | 76.9        | 50.0        | 49.6        | 67.7        | 1.9         | 76.8        | 88.9        | 58.7        | 74.8        | 17.1        | 51.6        | 62.1        | 94.2        | 58.8        | <b>76.5</b>  | 72.4        | 68.3        | 39.8        | <b>63.3</b>   | 57.6         | 54.5          | <b>77.8</b>      | 41.9         | 54.6        | 46.6        | 33.7 | 65.9        |
| LR-VGG-16     | 76.3        | 82.5           | 19.9        | 74.7        | 71.0        | 26.6        | 82.5        | 86.8        | 86.4        | 70.7        | 41.4        | 41.0        | 65.1        | <b>11.0</b> | 72.0        | 87.5        | 52.5        | 73.1        | 10.4        | 57.4        | 58.5        | 93.5        | 56.3        | 70.7         | 71.2        | 62.7        | 27.3        | 58.1          | 51.6         | 50.5          | 69.0             | 43.9         | 52.0        | 45.9        | 30.5 | 62.5        |
| LR-ResNet-50  | 78.5        | 88.2           | 24.6        | 80.8        | 75.9        | 44.2        | 83.8        | 88.7        | <b>87.8</b> | 76.2        | 50.9        | 48.1        | 67.4        | 0.9         | 77.1        | 88.8        | 57.3        | 76.8        | <b>29.3</b> | 57.5        | 63.3        | 94.2        | 61.0        | 72.4         | 73.0        | 70.5        | 42.1        | 62.3          | 64.8         | 55.1          | 72.0             | 48.7         | 55.9        | 48.9        | 36.4 | 67.3        |



TABLE IV  
EXAMPLE PREDICTIONS OF RESNEXT-101 ON THE MULTISCENE-CLEAN DATASET.

|                                                           |                                                                                   |                                                                                              |                                                                                    |                                                                                                                                       |                                                                                                                      |
|-----------------------------------------------------------|-----------------------------------------------------------------------------------|----------------------------------------------------------------------------------------------|------------------------------------------------------------------------------------|---------------------------------------------------------------------------------------------------------------------------------------|----------------------------------------------------------------------------------------------------------------------|
| Multi-scene Aerial Images in the MultiScene-Clean dataset |  |             |  |                                                    |                                   |
| Ground Truths                                             | bridge, parking lot, river, roundabout, and residential                           | woodland, lake/pond, and wastewater plant                                                    | bridge, parking lot, river, roundabout, and residential                            | farmland, woodland, orchard, residential, and sparse shrub                                                                            | lake/pond and quarry                                                                                                 |
| Predictions                                               | bridge, parking lot, river, roundabout, and residential                           | woodland, lake/pond, and wastewater plant                                                    | bridge, parking lot, river, roundabout, and residential                            | farmland, woodland, orchard, residential, and sparse shrub                                                                            | lake/pond and quarry                                                                                                 |
| Multi-scene Aerial Images in the MultiScene-Clean dataset |  |             |  |                                                    |                                   |
| Ground Truths                                             | commercial, farmland, parking lot, and residential                                | commercial, parking lot, park, railway, residential, train station, and works                | farmland, woodland, sparse shrub                                                   | baseball field, basketball field, lake/pond, parking lot, residential, soccer field, and tennis court                                 | bridge, commercial, parking lot, park, residential, river, roundabout, and solar farm                                |
| Predictions                                               | commercial, farmland, <b>woodland</b> , <b>parking lot</b> , and residential      | commercial, parking lot, <b>park</b> , railway, residential, train station, and <b>works</b> | farmland, woodland, <b>lake/pond</b> , and sparse shrub                            | <b>baseball field</b> , <b>basketball field</b> , lake/pond, <b>parking lot</b> , residential, <b>soccer field</b> , and tennis court | bridge, commercial, <b>lake/pond</b> , parking lot, <b>park</b> , <b>river</b> , <b>solar farm</b> , and residential |

Purple predictions indicate false negatives, while blue predictions are false positives.

channels for enabling information to flow across channels belonging to different groups. Besides, element-wise addition, which is often used in a residual block, is replaced with concatenation for enlarging channel dimension at a low computational cost. In ShuffleNet-V2 [78], features are grouped by channel split, and pointwise group convolutions are discarded. As a consequence, two feature groups are yielded and fed into two branches, of which one is an identity mapping and the other is a set of convolutions. Afterwards, outputs are concatenated and shuffled along the channel dimension. In our experiments, we evaluate the performance of ShuffleNet-V2 on our dataset.

- *DenseNet* [79]: DenseNet proposes to enhance information flow by directly connecting each layer to all subsequent layers with equivalent feature-map sizes. To preserve information learned by proceeding layers, concatenation is employed to combine features from various layers. By reusing feature maps throughout entire networks, DenseNet can learn compact internal representations for visual recognition tasks. Two variations, a 121-layer DenseNet (DenseNet-121) and a 169-layer DenseNet (DenseNet-169), are tested.
- *ResNeXt* [80]: ResNeXt learns residuals with aggre-

gated residual transformations but not a stack of convolutional layers (e.g., ResNet). The aggregated residual transformation is implemented by first slicing features into low-dimensional embeddings and then conducting convolutions on them. Afterwards, outputs are aggregated with element-wise addition. With this design, ResNeXt outperforms its ResNet counterpart on ImageNet-5K [80] and COCO [81] datasets. We test a 50-layer ResNeXt (ResNeXt-50) and a 101-layer (ResNeXt-101) in our experiments.

- *MnasNet* [82]: MnasNet architectures are automatically learned on target datasets through a mobile neural architecture search (MNAS) algorithm [82]. Compared to conventional NAS algorithms [83], MNAS takes not only classification accuracy but also model latency into consideration and is executed on mobile phones for measuring real-world inference latency. As a consequence, MnasNet searched on target datasets is expected to achieve a good trade-off between accuracy and latency. To control the model size, a depth multiplier is designed for scaling the number of channels in each layer. In our experiments, the depth multiplier is set to 1, and the best-performing MnasNet searched on the ImageNet dataset [84] is chosen to perform multi-scene recognition in the wild.

TABLE V  
NUMERICAL RESULTS OF BASELINE MODELS ON THE MULTISCENE DATASET (%). MODELS ARE TRAINED ON IMAGES WITH NOISY CROWDSOURCED ANNOTATIONS AND TESTED ON CLEANLY-LABELED IMAGES. THE BEST SCORES ARE SHOWN IN BOLD.

| Model         | mAP         | mCP         | mCR         | mCF <sub>1</sub> | mEP         | mER         | mEF <sub>1</sub> | OP          | OR          | OF <sub>1</sub> |
|---------------|-------------|-------------|-------------|------------------|-------------|-------------|------------------|-------------|-------------|-----------------|
| SVM           | 14.7        | 24.7        | 4.1         | 5.4              | 51.4        | 15.7        | 23.1             | 77.7        | 15.5        | 25.8            |
| RF            | 15.1        | 49.7        | 4.4         | 6.1              | 55.4        | 16.4        | 34.3             | 78.7        | 15.8        | 26.3            |
| XGBOOST       | 18.4        | 54.6        | 10.6        | 14.9             | 62.0        | 26.7        | 35.1             | 70.4        | 25.5        | 37.4            |
| VGG-16        | 63.4        | 71.0        | 46.9        | 54.1             | 78.4        | 51.6        | 59.3             | 79.3        | 49.6        | 61.0            |
| VGG-19        | 59.8        | 68.9        | 47.2        | 54.1             | 75.5        | 52.2        | 58.9             | 75.1        | 50.2        | 60.2            |
| Inception-V3  | 65.8        | 74.1        | 50.8        | 58.5             | 79.1        | 53.8        | 61.2             | 79.5        | 51.9        | 62.8            |
| ResNet-50     | 63.9        | 73.7        | 47.7        | 55.9             | 78.3        | 52.5        | 60.0             | 78.5        | 50.7        | 61.6            |
| ResNet-101    | 63.4        | 73.0        | 47.5        | 55.5             | 77.1        | 52.5        | 59.7             | 77.2        | 50.6        | 61.2            |
| ResNet-152    | 62.8        | 73.2        | 47.6        | 55.7             | 76.2        | 53.1        | 59.9             | 76.5        | 51.3        | 61.4            |
| SqueezeNet    | 61.4        | 74.4        | 41.1        | 50.5             | 78.9        | 47.7        | 56.4             | 80.7        | 45.9        | 58.5            |
| MobileNet-V2  | 65.5        | 72.3        | 48.4        | 56.0             | 79.6        | 54.6        | 62.0             | 80.1        | 52.8        | 63.6            |
| ShuffleNet-V2 | 65.1        | 74.6        | 46.7        | 55.1             | 81.7        | 51.0        | 59.9             | <b>82.9</b> | 49.0        | 61.6            |
| DenseNet-121  | 67.5        | 77.0        | 49.4        | 58.2             | <b>82.2</b> | 54.4        | <b>62.6</b>      | 82.8        | 52.3        | <b>64.1</b>     |
| DenseNet-169  | 64.2        | 71.3        | <b>53.3</b> | <b>59.3</b>      | 77.2        | <b>55.7</b> | 62.0             | 77.1        | <b>53.9</b> | 63.4            |
| ResNeXt-50    | 63.9        | 73.6        | 49.0        | 56.9             | 77.5        | 52.6        | 59.8             | 77.6        | 50.7        | 61.3            |
| ResNeXt-101   | 60.8        | 68.5        | 47.4        | 53.7             | 73.8        | 51.2        | 57.7             | 74.0        | 49.5        | 59.3            |
| MnasNet       | 58.1        | 74.1        | 31.0        | 40.4             | 75.0        | 38.0        | 47.6             | 80.4        | 36.0        | 49.7            |
| KFBNet        | 67.1        | <b>77.7</b> | 46.2        | 54.3             | 80.2        | 54.0        | 61.7             | 81.1        | 52.3        | 63.6            |
| FACNN         | 65.2        | 73.9        | 47.6        | 55.6             | 78.9        | 53.9        | 61.1             | 80.0        | 52.1        | 63.1            |
| SAFF          | 64.8        | 74.0        | 47.4        | 55.3             | 80.9        | 51.2        | 59.8             | 81.8        | 49.4        | 61.6            |
| LR-VGG-16     | <b>67.8</b> | 76.0        | 48.4        | 56.1             | 80.5        | 52.1        | 60.5             | 81.3        | 50.3        | 62.2            |
| LR-ResNet-50  | 65.5        | 71.2        | 51.6        | 57.9             | 79.2        | 53.1        | 60.7             | 79.4        | 51.2        | 62.3            |

- *KFBNet* [51]: KFBNet exploits a key region capturing method namely key filter bank (KFB) for aerial image scene classification. The proposed KFB is composed of two streams: a global stream (G-Stream) and a key stream (K-Stream). The former predicts labels using features learned by the last block of a CNN, while the latter highlights key features in both spatial and channel dimensions for inferring scene categories. Finally, predictions made by the two streams are merged via an element-wise addition as the final decision. We take VGG-16 as the backbone and report numerical results in Table II, III, and V.
- *FACNN* [52]: FACNN is a scene classification network composed of a CNN backbone and a Feature Aggregation module. In the latter, features extracted by the last three blocks of VGG-16 are aggregated through pooling operations and  $1 \times 1$  convolutions. Afterwards, they are concatenated with outputs of the second fully-connected layer of VGG-16 to form discriminative scene representations for the final prediction.
- *SAFF* [53]: SAFF proposes a non-parametric self-attention layer for enhancing spatial and channel responses of feature maps. Specifically, features extracted by the last three blocks of a pre-trained CNN (e.g., VGG-16) are fused and fed into the proposed self-attention layer. In this layer, spatial- and channel-wise weightings are conducted to emphasize the importance of locations of salient objects and channels with infrequently occurring features, respectively. Principal component analysis (PCA) whitening is also introduced to reduce the information redundancy and squash channels. However, since this operation frequently fails the network training, we replace it with a learnable fully-connected layer. Besides, VGG-16 is selected as the backbone in our experiments.
- *LR-CNN* [58]: LR-CNN is a multi-label classification

network, which consists of three elements: a class-wise feature extraction module, an attentional region extraction module, and a relational reasoning module. Specifically, the first module learns deep features with respect to each category from the input images. Afterwards, the second module extracts attentional regions of class-wise features, which are eventually leveraged to reason about relations between different objects for inferring their existences through the third module. In our experiments, we validate LR-VGG-16 and LR-ResNet-50, where VGG-16 and ResNet-50 are taken as backbones, respectively.

### C. Training Details

Before training SVM, RF, and XGBOOST, we use histogram of oriented gradient (HOG) [85] and local binary pattern (LBP) [86] as visual features as recommended in [87]. The size of each cell is set to  $32 \times 32$  pixels for HOG, and the radius is defined as 16 pixels for LBP. We use Scipy to implement these machine learning classifiers and apply them to multi-scene recognition using the function *MultiOutputClassifier*<sup>5</sup>. As to baseline classification neural networks, we initialize them with weights pre-trained on the ImageNet dataset and fine-tune them on the proposed multi-scene image dataset. The loss is defined as binary cross-entropy, and stochastic gradient descent (SGD) with momentum [88] is selected as the optimizer. To accelerate the network convergence, the momentum is set to a large value, 0.9. Besides, the initial learning rate and weight decay are set to 0.02 and  $1e-4$ , respectively. All deep networks are implemented on Pytorch and validated on one NVIDIA Tesla V100-SXM2 32GB GPU. For experiments on both MultiScene-Clean and MultiScene, we train networks for 87k and 581k iterations, respectively,

<sup>5</sup><https://scikit-learn.org/stable/modules/generated/sklearn.multioutput.MultiOutputClassifier.html>

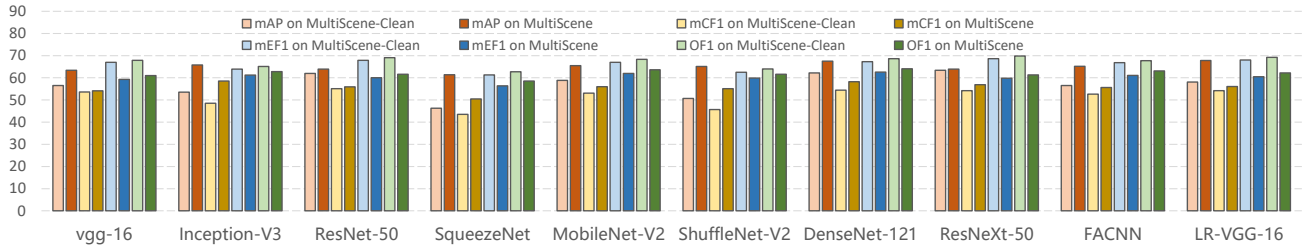


Fig. 7. Comparisons of the performance of networks trained on images with clean (light-color bars) and crowdsourced (dark-color bars) annotations, respectively. For each network, the left four bars represent class-based scores, mAPs and CF<sub>1</sub>, while the right four bars indicate EF<sub>1</sub> and OF<sub>1</sub> scores.

and the size of each training batch is set to 16 for both versions.

#### D. Experimental Results across Different Tasks

1) *Multi-scene Recognition with Cleanly-labeled Data*: To evaluate baselines for our task, we conduct experiments on the MultiScene-Clean dataset and report quantitative results in Table II. It can be seen that ResNeXt-101 achieves the best mAP (64.8%), mEF<sub>1</sub> (70.2%), and OF<sub>1</sub> score (71.3%), which demonstrate its high performance and robustness in this task from almost all perspectives. LR-ResNet-50 gains the highest value in mCF<sub>1</sub> (59.0%) owing to its capability of reasoning about relations among various scenes. Moreover, such a reasoning capability also enables LR-ResNet-50 to surpass the other baselines in all recall metrics, as scenes tend to be predicted as positive once its related scenes are recognized. Another observation is that MnasNet, SqueezeNet, and ShuffleNet-V2 show relatively poor performance due to their light-weight designs. Compared to deep neural networks, traditional machine learning algorithms achieve lower scores in all metrics.

For an insight into the performance of networks in identifying different scenes, we also report per-class APs in Table III. As we can see, ResNeXt-101 achieves the highest APs in most scenes, which is in line with the previous observations. Furthermore, we note that most networks fail to accurately recognize scenes having scarce training samples, e.g., oil field and port. This suggests that learning unbiased models on an imbalanced dataset is a big challenge. Besides numerical results, we exhibit several predictions in Table IV.

2) *Learning from Noisy Crowdsourced Labels*: We investigate networks learned from noisy crowdsourced labels for our task on the MultiScene dataset. To ensure a fair comparison, we utilize the same test set as in Section IV-D and report numerical results in Table V. It can be observed that OF<sub>1</sub> scores of all models are decreased by an average of 8.2% compared to the values in Table II, which demonstrates that noise in crowdsourced annotations significantly affects the learning of deep neural networks. Moreover, it is interesting to note that the values of class-based metrics, mAP and mCF<sub>1</sub> score, are increased by 4.6% and 1.2%, respectively, in comparison with those in Table II. This can be attributed to the fact that numbers of training samples, especially for scenes seldomly appearing, are effortlessly increased by crawling OSM data with keyword searching. Compared to models showing high performance on

the MultiScene-Clean dataset, we find that DenseNet gains the highest scores in mCF<sub>1</sub> (59.3%), mEF<sub>1</sub> (62.6%), and mOF<sub>1</sub> (64.1%), as it can sufficiently reuse features and has relatively few parameters. Besides, LR-VGG-16 achieves the highest mAP (67.8%), which demonstrates that taking advantage of underlying relations among various scenes can suppress the influence of noise introduced by OSM data. Furthermore, we compare the performance of several networks trained on MultiScene-Clean and MultiScene datasets in Fig. 7, and it can be again observed that higher class-based scores (see orange and brown bars in Fig. 7) are obtained when using massive crowdsourced labels. All in all, although crowdsourced labels influence the overall performance of networks, comparisons in class-based scores also suggest their great potential.

#### V. CONCLUSION

In this paper, we propose a large-scale dataset, MultiScene, for multi-scene recognition in single images, which is featured by unconstrained multi-scene aerial images and the available both crowdsourced and clean labels. The proposed dataset allows researches in not only recognizing aerial scenes in the wild but also learning from noisy crowdsourced labels. We comprehensively evaluate popular baseline models on both MultiScene-Clean (a subset consisting of only cleanly-labeled images) and MultiScene datasets. Experimental results on the former demonstrate that unconstrained multi-scene recognition is still a challenging task, and those on the latter showcase the great potential of exploiting a large number of crowdsourced annotations. Looking into the future, the dataset can be applied to develop more efficient networks and learning strategies for exploiting noisy labels for aerial scene understanding in the wild.

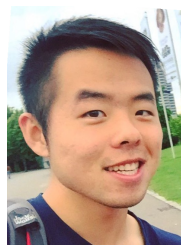
#### REFERENCES

- [1] Q. Weng, Z. Mao, J. Lin, and X. Liao, "Land-use scene classification based on a CNN using a constrained extreme learning machine," *International Journal of Remote Sensing*, pp. 1–19, 2018.
- [2] G. Cheng, J. Han, and X. Lu, "Remote sensing image scene classification: Benchmark and state of the art," *Proceedings of the IEEE*, vol. 105, no. 10, pp. 1865–1883, 2017.
- [3] D. Wen, X. Huang, H. Liu, W. Liao, and L. Zhang, "Semantic classification of urban trees using very high resolution satellite imagery," *IEEE Journal of Selected Topics in Applied Earth Observations and Remote Sensing*, vol. 10, no. 4, pp. 1413–1424, 2017.
- [4] S. Manfreda, M. McCabe, P. Miller, R. Lucas, V. Pajuelo Madrigal, G. Mallinis, E. Ben Dor, D. Helman, L. Estes, G. Ciraolo, J. Müllerová, F. Tauro, M. De Lima, L. De Lima, A. Maltese, F. Frances, K. Caylor, M. Kohv, M. Perks, G. Ruiz-Pérez, Z. Su, G. Vico, and B. Toth, "On the use of unmanned aerial systems for environmental monitoring," *Remote sensing*, vol. 10, no. 4, p. 641, 2018.

- [5] L. Mou and X. X. Zhu, "IM2HEIGHT: Height estimation from single monocular imagery via fully residual convolutional-deconvolutional network," *arXiv:1802.10249*, 2018.
- [6] C. Qiu, L. Mou, M. Schmitt, and X. X. Zhu, "Local climate zone-based urban land cover classification from multi-seasonal Sentinel-2 images with a recurrent residual network," *ISPRS Journal of Photogrammetry and Remote Sensing*, vol. 154, pp. 151–162, 2019.
- [7] D. Marmanis, K. Schindler, J. D. Wegner, S. Galliani, M. Datcu, and U. Stilla, "Classification with an edge: Improving semantic image segmentation with boundary detection," *ISPRS Journal of Photogrammetry and Remote Sensing*, vol. 135, pp. 158–172, 2018.
- [8] N. Audebert, B. L. Saux, and S. Lefèvre, "Beyond RGB: Very high resolution urban remote sensing with multimodal deep networks," *ISPRS Journal of Photogrammetry and Remote Sensing*, vol. 140, pp. 20–32, 2018.
- [9] L. Mou and X. X. Zhu, "RiFCN: Recurrent network in fully convolutional network for semantic segmentation of high resolution remote sensing images," *arXiv:1805.02091*, 2018.
- [10] Q. Li, L. Mou, Q. Liu, Y. Wang, and X. X. Zhu, "HSF-Net: Multi-scale deep feature embedding for ship detection in optical remote sensing imagery," *IEEE Transactions on Geoscience and Remote Sensing*, 2017.
- [11] C. Qiu, M. Schmitt, C. Geiß, T. Chen, and X. X. Zhu, "A framework for large-scale mapping of human settlement extent from Sentinel-2 images via fully convolutional neural networks," *ISPRS Journal of Photogrammetry and Remote Sensing*, vol. 163, pp. 152–170, 2020.
- [12] Q. Li, Y. Shi, X. Huang, and X. X. Zhu, "Building footprint generation by integrating convolution neural network with feature pairwise conditional random field (FPCRF)," *IEEE Transactions on Geoscience and Remote Sensing*, 2020.
- [13] G. Cheng, L. Guo, T. Zhao, J. Han, H. Li, and J. Fang, "Automatic landslide detection from remote-sensing imagery using a scene classification method based on BoVW and pLSA," *International Journal of Remote Sensing*, vol. 34, no. 1, pp. 45–59, 2013.
- [14] Q. Zhu, Y. Zhong, B. Zhao, G. S. Xia, and L. Zhang, "Bag-of-visual-words scene classifier with local and global features for high spatial resolution remote sensing imagery," *IEEE Geoscience and Remote Sensing Letters*, vol. 13, no. 6, pp. 747–751, 2016.
- [15] G. Cheng, C. Yang, X. Yao, L. Guo, and J. Han, "When deep learning meets metric learning: Remote sensing image scene classification via learning discriminative cnns," *IEEE transactions on geoscience and remote sensing*, vol. 56, no. 5, pp. 2811–2821, 2018.
- [16] D. Marcos, M. Volpi, B. Kellenberger, and D. Tuia, "Land cover mapping at very high resolution with rotation equivariant CNNs: Towards small yet accurate models," *ISPRS Journal of Photogrammetry and Remote Sensing*, vol. 145, pp. 96–107, 2018.
- [17] A. Vetrivel, M. Gerke, N. Kerle, F. Nex, and G. Vosselman, "Disaster damage detection through synergistic use of deep learning and 3D point cloud features derived from very high resolution oblique aerial images, and multiple-kernel-learning," *ISPRS Journal of Photogrammetry and Remote Sensing*, vol. 140, pp. 45–59, 2018.
- [18] W. Lee, S. Kim, Y. Lee, H. Lee, and M. Choi, "Deep neural networks for wild fire detection with unmanned aerial vehicle," in *IEEE International Conference on Consumer Electronics (ICCE)*, 2017.
- [19] D. Hu, X. Li, L. Mou, P. Jin, D. Chen, L. Jing, X. X. Zhu, and D. Dou, "Cross-task transfer for multimodal aerial scene recognition," in *European Conference on Computer Vision (ECCV)*, 2020.
- [20] H. Sun, S. Li, X. Zheng, and X. Lu, "Remote sensing scene classification by gated bidirectional network," *IEEE Transactions on Geoscience and Remote Sensing*, vol. 58, no. 1, pp. 82–96, 2020.
- [21] J. Murray, D. Marcos, and D. Tuia, "Zoom In, Zoom Out: Injecting scale invariance into landuse classification CNNs," in *IEEE International Geoscience and Remote Sensing Symposium (IGARSS)*, 2019.
- [22] G. Cheng, X. Xie, J. Han, L. Guo, and G. Xia, "Remote sensing image scene classification meets deep learning: Challenges, methods, benchmarks, and opportunities," *IEEE Journal of Selected Topics in Applied Earth Observations and Remote Sensing*, vol. 13, pp. 3735–3756, 2020.
- [23] A. Byju, G. Sumbul, B. Demir, and L. Bruzzone, "Remote sensing image scene classification with deep neural networks in JPEG 2000 compressed domain," *arXiv:2006.11529*, 2020.
- [24] Y. Xu, B. Du, and L. Zhang, "Assessing the threat of adversarial examples on deep neural networks for remote sensing scene classification: Attacks and defenses," *IEEE Transactions on Geoscience and Remote Sensing*, 2020.
- [25] L. Ru, B. Du, and C. Wu, "Multi-temporal scene classification and scene change detection with correlation based fusion," *arXiv:2006.02176*, 2020.
- [26] Q. Li, C. Qiu, L. Ma, M. Schmitt, and X. X. Zhu, "Mapping the land cover of Africa at 10 m resolution from multi-source remote sensing data with Google Earth engine," *Remote Sensing*, vol. 12, no. 4, p. 602, 2020.
- [27] G. Xia, J. Hu, F. Hu, B. Shi, X. Bai, Y. Zhong, L. Zhang, and X. Lu, "AID: A benchmark data set for performance evaluation of aerial scene classification," *IEEE Transactions on Geoscience and Remote Sensing*, 2017.
- [28] P. Jin, G. Xia, F. Hu, Q. Lu, and L. Zhang, "AID++: An updated version of aid on scene classification," in *IEEE International Geoscience and Remote Sensing Symposium (IGARSS)*, 2018.
- [29] D. Tuia, D. Marcos, and G. Camps-Valls, "Multi-temporal and multi-source remote sensing image classification by nonlinear relative normalization," *ISPRS Journal of Photogrammetry and Remote Sensing*, vol. 120, pp. 1–12, 2016.
- [30] S. Niazmardi, B. Demir, L. Bruzzone, A. Safari, and S. Homayouni, "Multiple kernel learning for remote sensing image classification," *IEEE Transactions on Geoscience and Remote Sensing*, vol. 56, no. 3, pp. 1425–1443, 2017.
- [31] Q. Bi, K. Qin, Z. Li, H. Zhang, K. Xu, and G. Xia, "A multiple-instance densely-connected ConvNet for aerial scene classification," *IEEE Transactions on Image Processing*, vol. 29, pp. 4911–4926, 2020.
- [32] J. Lin, L. Mou, T. Yu, X. X. Zhu, and Z. J. Wang, "Dual adversarial network for unsupervised ground/satellite-to-aerial scene adaptation," in *ACM International Conference on Multimedia (ACMMM)*, 2020.
- [33] X. Wang, X. Xiong, and C. Ning, "Multi-label remote sensing scene classification using multi-bag integration," *IEEE Access*, vol. 7, pp. 120 399–120 410, 2019.
- [34] Q. Zhu, X. Sun, Y. Zhong, and L. Zhang, "High-resolution remote sensing image scene understanding: A review," in *IEEE International Geoscience and Remote Sensing Symposium (IGARSS)*, 2019.
- [35] Y. Long, G. Xia, S. Li, W. Yang, M. Yang, X. X. Zhu, L. Zhang, and D. Li, "DIRS: On creating benchmark datasets for remote sensing image interpretation," *arXiv:2006.12485*, 2020.
- [36] S. Zorzi and F. Fraundorfer, "Regularization of building boundaries in satellite images using adversarial and regularized losses," in *IEEE International Geoscience and Remote Sensing Symposium (IGARSS)*, 2019.
- [37] Y. Yang and S. Newsam, "Bag-of-visual-words and spatial extensions for land-use classification," in *ACM SIGSPATIAL International Conference on Advances in Geographic Information Systems*, 2010.
- [38] J. Hu, T. Jiang, X. Tong, G. Xia, and L. Zhang, "A benchmark for scene classification of high spatial resolution remote sensing imagery," in *IEEE International Geoscience and Remote Sensing Symposium (IGARSS)*, 2015.
- [39] Q. Zou, L. Ni, T. Zhang, and Q. Wang, "Deep learning based feature selection for remote sensing scene classification," *IEEE Geoscience and Remote Sensing Letters*, vol. 12, no. 11, pp. 2321–2325, 2015.
- [40] G. Cheng, J. Han, and X. Lu, "Remote sensing image scene classification: Benchmark and state of the art," *Proceedings of the IEEE*, vol. 105, no. 10, pp. 1865–1883, 2017.
- [41] D. Lowe, "Distinctive image features from scale-invariant keypoints," *International Journal of Computer Vision*, vol. 60, no. 2, pp. 91–110, 2004.
- [42] V. Risojević, S. Momić, and Z. Babić, "Gabor descriptors for aerial image classification," in *International Conference on Adaptive and Natural Computing Algorithms*, 2011.
- [43] M. Swain and D. Ballard, "Color indexing," *International Journal of Computer Vision*, vol. 7, no. 1, pp. 11–32, 1991.
- [44] J. dos Santos, O. Penatti, and R. da Silva Torres, "Evaluating the potential of texture and color descriptors for remote sensing image retrieval and classification," in *International Conferences on Computer Vision Theory and Applications (VISAPP)*, 2010.
- [45] B. Manjunath and W. Ma, "Texture features for browsing and retrieval of image data," *IEEE Transactions on Pattern Analysis and Machine Intelligence*, vol. 18, no. 8, pp. 837–842, 1996.
- [46] V. Risojević and Z. Babić, "Aerial image classification using structural texture similarity," in *IEEE International Symposium on Signal Processing and Information Technology (ISSPIT)*, 2011.
- [47] Y. Yang and S. Newsam, "Bag-of-visual-words and spatial extensions for land-use classification," in *International Conference on Advances in Geographic Information Systems (SIGSPATIAL)*, 2010.
- [48] L. Zhao, P. Tang, and L. Huo, "Land-use scene classification using a concentric circle-structured multiscale bag-of-visual-words model," *IEEE Journal of Selected Topics in Applied Earth Observations and Remote Sensing*, vol. 7, no. 12, pp. 4620–4631, 2014.



- [49] M. Lienou, H. Maitre, and M. Datcu, "Semantic annotation of satellite images using latent dirichlet allocation," *IEEE Geoscience and Remote Sensing Letters*, vol. 7, no. 1, pp. 28–32, 2009.
- [50] Y. Zhong, Q. Zhu, and L. Zhang, "Scene classification based on the multifeature fusion probabilistic topic model for high spatial resolution remote sensing imagery," *IEEE Transactions on Geoscience and Remote Sensing*, vol. 53, no. 11, pp. 6207–6222, 2015.
- [51] F. Li, R. Feng, W. Han, and L. Wang, "High-resolution remote sensing image scene classification via key filter bank based on convolutional neural network," *IEEE Transactions on Geoscience and Remote Sensing*, vol. 58, no. 11, pp. 8077–8092, 2020.
- [52] X. Lu, H. Sun, and X. Zheng, "A feature aggregation convolutional neural network for remote sensing scene classification," *IEEE Transactions on Geoscience and Remote Sensing*, vol. 57, no. 10, pp. 7894–7906, 2019.
- [53] R. Cao, L. Fang, T. Lu, and N. He, "Self-attention-based deep feature fusion for remote sensing scene classification," *IEEE Geoscience and Remote Sensing Letters*, vol. 18, no. 1, pp. 43–47, 2020.
- [54] A. Zeggada, F. Melgani, and Y. Bazi, "A deep learning approach to UAV image multilabeling," *IEEE Geoscience and Remote Sensing Letters*, vol. 14, no. 5, pp. 694–698, 2017.
- [55] A. Zeggada, S. Benbraika, F. Melgani, and Z. Mokhtari, "Multilabel conditional random field classification for UAV images," *IEEE Geoscience and Remote Sensing Letters*, vol. 15, no. 3, pp. 399–403, 2018.
- [56] Y. Hua, L. Mou, and X. X. Zhu, "Recurrently exploring class-wise attention in a hybrid convolutional and bidirectional LSTM network for multilabel aerial image classification," *ISPRS Journal of Photogrammetry and Remote Sensing*, vol. 149, pp. 188–199, 2019.
- [57] G. Sumbul and B. Demir, "A deep multi-attention driven approach for multi-label remote sensing image classification," *IEEE Access*, vol. 8, pp. 95 934–95 946, 2020.
- [58] Y. Hua, L. Mou, and X. X. Zhu, "Relation network for multilabel aerial image classification," *IEEE Transactions on Geoscience and Remote Sensing*, vol. 58, no. 7, pp. 4558–4572, 2020.
- [59] S. Koda, A. Zeggada, F. Melgani, and R. Nishii, "Spatial and structured SVM for multilabel image classification," *IEEE Transactions on Geoscience and Remote Sensing*, vol. 56, no. 10, pp. 5948–5960, 2018.
- [60] B. Chaudhuri, B. Demir, S. Chaudhuri, and L. Bruzzone, "Multilabel remote sensing image retrieval using a semisupervised graph-theoretic method," *IEEE Transactions on Geoscience and Remote Sensing*, vol. 56, no. 2, pp. 1144–1158, 2017.
- [61] G. Xia, W. Yang, J. Delon, Y. Gousseau, H. Sun, and H. Maitre, "Structural high-resolution satellite image indexing," in *ISPRS TC VII Symposium*, 2010.
- [62] G. Sumbul, M. Charfuelan, B. Demir, and V. Markl, "BigEarthNet: A large-scale benchmark archive for remote sensing image understanding," in *IEEE International Geoscience and Remote Sensing Symposium (IGARSS)*, 2019.
- [63] C. Cortes and V. Vapnik, "Support-vector networks," *Machine Learning*, vol. 20, no. 3, pp. 273–297, 1995.
- [64] J. Vert, K. Tsuda, and B. Schölkopf, "A primer on kernel methods," *Kernel Methods in Computational Biology*, vol. 47, pp. 35–70, 2004.
- [65] T. Ho, "Random decision forests," in *International Conference on Document Analysis and Recognition*, 1995.
- [66] T. Hastie, R. Tibshirani, and J. Friedman, "Boosting and additive trees," in *The Elements of Statistical Learning*, 2009.
- [67] J. Friedman, "Greedy function approximation: a gradient boosting machine," *Annals of Statistics*, pp. 1189–1232, 2001.
- [68] K. Simonyan and A. Zisserman, "Very deep convolutional networks for large-scale image recognition," *arXiv:1409.1556*, 2014.
- [69] C. Szegedy, W. Liu, Y. Jia, P. Sermanet, S. Reed, D. Anguelov, D. Erhan, V. Vanhoucke, and A. Rabinovich, "Going deeper with convolutions," in *IEEE Conference on Computer Vision and Pattern Recognition (CVPR)*, 2015.
- [70] S. Ioffe and C. Szegedy, "Batch normalization: Accelerating deep network training by reducing internal covariate shift," in *International Conference on Machine Learning (ICML)*, 2015.
- [71] C. Szegedy, V. Vanhoucke, S. Ioffe, J. Shlens, and Z. Wojna, "Rethinking the Inception architecture for computer vision," in *IEEE Conference on Computer Vision and Pattern Recognition (CVPR)*, 2016.
- [72] C. Szegedy, S. Ioffe, V. Vanhoucke, and A. A. Alemi, "Inception-v4, Inception-ResNet and the impact of residual connections on learning," in *AAAI Conference on Artificial Intelligence (AAAI)*, 2017.
- [73] K. He, X. Zhang, S. Ren, and J. Sun, "Deep residual learning for image recognition," in *IEEE Conference on Computer Vision and Pattern Recognition (CVPR)*, 2016.
- [74] F. Iandola, S. Han, M. Moskewicz, K. Ashraf, W. Dally, and K. Keutzer, "SqueezeNet: AlexNet-level accuracy with 50x fewer parameters and 0.5 MB model size," in *International Conference on Learning Representations (ICLR)*, 2017.
- [75] A. Howard, M. Zhu, B. Chen, D. Kalenichenko, W. Wang, T. Weyand, M. Andreetto, and H. Adam, "Mobilenets: Efficient convolutional neural networks for mobile vision applications," *arXiv:1704.04861*, 2017.
- [76] M. Sandler, A. Howard, M. Zhu, A. Zhmoginov, and L. Chen, "Mobilenets: Efficient convolutional neural networks for mobile vision applications," in *IEEE Conference on Computer Vision and Pattern Recognition (CVPR)*, 2018.
- [77] X. Zhang, X. Zhou, M. Lin, and J. Sun, "ShuffleNet: An extremely efficient convolutional neural network for mobile devices," in *IEEE Conference on Computer Vision and Pattern Recognition (CVPR)*, 2018.
- [78] N. Ma, X. Zhang, H. Zheng, and J. Sun, "ShuffleNetV2: Practical guidelines for efficient cnn architecture design," in *European Conference on Computer Vision (ECCV)*, 2018.
- [79] G. Huang, Z. Liu, L. V. D. Maaten, and K. Weinberger, "Densely connected convolutional networks," in *IEEE Conference on Computer Vision and Pattern Recognition (CVPR)*, 2017.
- [80] S. Xie, R. Girshick, P. Dollár, Z. Tu, and K. He, "Aggregated residual transformations for deep neural networks," in *IEEE Conference on Computer Vision and Pattern Recognition (CVPR)*, 2017.
- [81] T. Lin, M. Maire, S. Belongie, J. Hays, P. Perona, D. Ramanan, P. Dollár, and C. Zitnick, "Microsoft COCO: Common objects in context," in *European Conference on Computer Vision (ECCV)*, 2014.
- [82] M. Tan, B. Chen, R. Pang, V. Vasudevan, M. Sandler, A. Howard, and Q. Le, "MnasNet: Platform-aware neural architecture search for mobile," in *IEEE Conference on Computer Vision and Pattern Recognition (CVPR)*, 2019.
- [83] B. Zoph and Q. Le, "Neural architecture search with reinforcement learning," in *International Conference on Learning Representations (ICLR)*, 2017.
- [84] J. Deng, W. Dong, R. Socher, L. Li, K. Li, and F. Li, "ImageNet: A large-scale hierarchical image database," in *IEEE Conference on Computer Vision and Pattern Recognition (CVPR)*, 2009.
- [85] N. Dalal and B. Triggs, "Histograms of oriented gradients for human detection," in *IEEE Conference on Computer Vision and Pattern Recognition (CVPR)*, 2005.
- [86] T. Ojala, M. Pietikainen, and T. Maenpää, "Multiresolution gray-scale and rotation invariant texture classification with local binary patterns," *IEEE Transactions on Pattern Analysis and Machine Intelligence*, vol. 24, no. 7, pp. 971–987, 2002.
- [87] Y. Lin, F. Lv, S. Zhu, M. Yang, T. Cour, K. Yu, L. Cao, and T. Huang, "Large-scale image classification: fast feature extraction and SVM training," in *IEEE Conference on Computer Vision and Pattern Recognition (CVPR)*, 2011.
- [88] I. Sutskever, J. Martens, G. Dahl, and G. Hinton, "On the importance of initialization and momentum in deep learning," in *International Conference on Machine Learning (ICML)*, 2013.



**Yuansheng Hua** (S'18) received the bachelor's degree in remote sensing science and technology from the Wuhan University, Wuhan, China, in 2014, and double master's degrees in Earth Oriented Space Science and Technology (ESPACE) and Photogrammetry and remote sensing from the Technical University of Munich (TUM), Munich, Germany, and Wuhan University, Wuhan, China, in 2018 and 2019, respectively. He is currently pursuing the Ph.D. degree with the German Aerospace Center (DLR), Wessling, Germany and the Technical University of Munich (TUM), Munich, Germany.

In 2019, he was a visiting researcher with the Wageningen University & Research, Wageningen, Netherlands. His research interests include remote sensing, computer vision, and deep learning, especially their applications in remote sensing.



**Lichao Mou** received the Bachelor's degree in automation from the Xi'an University of Posts and Telecommunications, Xi'an, China, in 2012, the Master's degree in signal and information processing from the University of Chinese Academy of Sciences (UCAS), China, in 2015, and the Dr.-Ing. degree from the Technical University of Munich (TUM), Munich, Germany, in 2020.

He is currently a Guest Professor at the Munich AI Future Lab AI4EO, TUM and the Head of Visual Learning and Reasoning team at the Department "EO Data Science", Remote Sensing Technology Institute (IMF), German Aerospace Center (DLR), Weßling, Germany. Since 2019, he is a Research Scientist at DLR-IMF and an AI Consultant for the Helmholtz Artificial Intelligence Cooperation Unit (HAICU). In 2015 he spent six months at the Computer Vision Group at the University of Freiburg in Germany. In 2019 he was a Visiting Researcher with the Cambridge Image Analysis Group (CIA), University of Cambridge, UK.

He was the recipient of the first place in the 2016 IEEE GRSS Data Fusion Contest and finalists for the Best Student Paper Award at the 2017 Joint Urban Remote Sensing Event and 2019 Joint Urban Remote Sensing Event.



**Pu Jin** (S'21) received the bachelor's degree in electronic information science and technology from the Wuhan University, Wuhan, China, in 2017, and double master's degrees in Earth Oriented Space Science and Technology (ESPACE) and Photogrammetry and remote sensing from the Technical University of Munich (TUM), Munich, Germany, and Wuhan University, Wuhan, China, in 2020 and 2021, respectively. He is currently pursuing the Ph.D. degree with the German Aerospace Center (DLR), Weßling, Germany and the Technical University of

Munich (TUM), Munich, Germany. His research interests include remote sensing, computer vision, and deep learning, especially their applications in remote sensing.



**Xiao Xiang Zhu** (S'10–M'12–SM'14) received the Master (M.Sc.) degree, her doctor of engineering (Dr.-Ing.) degree and her "Habilitation" in the field of signal processing from Technical University of Munich (TUM), Munich, Germany, in 2008, 2011 and 2013, respectively.

She is currently the Professor for Signal Processing in Earth Observation ([www.sipeo.bgu.tum.de](http://www.sipeo.bgu.tum.de)) at Technical University of Munich (TUM) and German Aerospace Center (DLR); the head of the department "EO Data Science" at DLR's Earth Observation Center; and the head of the Helmholtz Young Investigator Group "SiPEO" at DLR and TUM. Since 2019, Zhu is co-coordinating the Munich Data Science Research School ([www.mu-ds.de](http://www.mu-ds.de)). She is also leading the Helmholtz Artificial Intelligence Cooperation Unit (HAICU) – Research Field "Aeronautics, Space and Transport". Prof. Zhu was a guest scientist or visiting professor at the Italian National Research Council (CNR-IREA), Naples, Italy, Fudan University, Shanghai, China, the University of Tokyo, Tokyo, Japan and University of California, Los Angeles, United States in 2009, 2014, 2015 and 2016, respectively. Her main research interests are remote sensing and Earth observation, signal processing, machine learning and data science, with a special application focus on global urban mapping.

Dr. Zhu is a member of young academy (Junge Akademie/Junges Kolleg) at the Berlin-Brandenburg Academy of Sciences and Humanities and the German National Academy of Sciences Leopoldina and the Bavarian Academy of Sciences and Humanities. She is an associate Editor of IEEE Transactions on Geoscience and Remote Sensing.